Beam-induced motion of vitrified specimen on holey carbon film

Axel F. Brilot [a], James Z. Chen [a,b,1], Anchi Cheng [c], Junhua Pan [d], Stephen C. Harrison [d,f], Clinton S. Potter [c], Bridget Carragher [c], Richard Henderson [e], Nikolaus Grigorieff [a,b,*]

[a] Department of Biochemistry, Rosenstiel Basic Medical Sciences Research Center, Brandeis University, MS029, 415 South Street, Waltham, MA 02454, USA
[b] Howard Hughes Medical Institute, Brandeis University, MS029, 415 South Street, Waltham, MA 02454, USA
[c] Department of Cell Biology, The Scripps Research Institute, La Jolla, CA 92037, USA
[d] Harvard Medical School and Children's Hospital, Boston, MA 02115, USA
[e] MRC Laboratory of Molecular Biology, Hills Road, Cambridge CB2 0QH, UK
[f] Department of Biological Chemistry and Molecular Pharmacology and Howard Hughes Medical Institute, Harvard Medical School, Boston, MA, USA

ARTICLE INFO

ABSTRACT

The contrast observed in images of frozen-hydrated biological specimens prepared for electron cryo-microscopy falls significantly short of theoretical predictions. In addition to limits imposed by the current instrumentation, it is widely acknowledged that motion of the specimen during its exposure to the electron beam leads to significant blurring in the recorded images. We have studied the amount and direction of motion of virus particles suspended in thin vitrified ice layers across holes in perforated carbon films using exposure series. Our data show that the particle motion is correlated within patches of 0.3–0.5 μm, indicating that the whole ice layer is moving in a drum-like motion, with accompanying particle rotations of up to a few degrees. Support films with smaller holes, as well as lower electron dose rates tend to reduce beam-induced specimen motion, consistent with a mechanical effect. Finally, analysis of movies showing changes in the specimen during beam exposure show that the specimen moves significantly more at the start of an exposure than towards its end. We show how alignment and averaging of movie frames can be used to restore high-resolution detail in images affected by beam-induced motion.

© 2012 Elsevier Inc. All rights reserved.

1. Introduction

Electron cryo-microscopy (cryo-EM) can be used to visualize the three-dimensional (3D) structure of a broad variety of specimens, including two-dimensional (2D) crystals (e.g., Gonen et al., 2004; Henderson et al., 1986), helical specimens (for example, Ge and Zhou, 2011; Miyazawa et al., 1999; Sachse et al., 2007; Yonekura et al., 2003) and isolated (single) particles. In recent years the application of the single particle approach has led to 3D reconstructions of a number of highly symmetrical virus particles at near-atomic resolution (4 Å or better, see Grigorieff and Harrison, 2011) for a recent review). Despite this success, it is commonly acknowledged that contrast in images of vitrified specimens falls significantly short of predicted physical limits (Glaeser, 1999; Henderson, 1995). Physical limits are imposed by the radiolysis of biological molecules caused by the high-energy electron beam which limits the electron dose to 5–10 electrons/$Å^2$ (Baker et al.,

2010; Henderson, 1992, 1995) if high-resolution features are to be preserved. Under idealized conditions, particle images are predicted to contain sufficient signal to obtain a 3D reconstruction at 3 Å resolution by averaging of a few thousand molecular images (Glaeser, 1999; Henderson, 1995). In practice however, the recent reconstructions of particles at near-atomic resolution have required averaging signal from several 100,000 to over 10 million images of subunits or asymmetric units (Grigorieff and Harrison, 2011). The contrast transfer function of the electron microscope, image detector noise and motion in the specimen induced by the incident electron beam all contribute to the loss of contrast in cryo-EM images (for a recent review, see Glaeser and Hall, 2011). The first two issues concern limitations of current instrumentation and are being addressed by technological improvements (Cambie et al., 2007; Danev and Nagayama, 2001; Majorovits et al., 2007; McMullan et al., 2009; Milazzo et al., 2011, 2005; Muller et al., 2010). Beam-induced specimen motion is thought to be caused by the reaction of the specimen to the high-energy electron beam, resulting in a build-up of positive charge on the specimen (Brink et al., 1998) and radiolysis of the sample and vitrified embedding medium (Glaeser, 2008; Glaeser and Taylor, 1978). Charge build-up leads to a weak deflection of the electron beam that can blur the image, especially of tilted samples in which the component of the deflection perpendicular to the beam is not zero (Glaeser and

Downing, 2004; Henderson, 1992). Radiolysis of the specimen is thought to lead to a build-up of internal pressure as the radiolysis products take up more space than the original molecules (Glaeser, 2008). The mechanical stress is sufficiently high to cause specimen deformations (and ultimately breakdown of the entire fabric – so-called bubbling), again blurring the final image. In a recent study, Glaeser and Henderson (Glaeser et al., 2011) studied the beam-induced motion of paraffin 2D crystals supported by a continuous carbon film and showed that film thicknesses greater than 35 nm significantly reduced the observed motion, thereby improving the fraction of images with strong high-resolution signal. These experiments further corroborate mechanical instability as one of the leading factors allowing beam-induced motion. Unfortunately, the use of a continuous carbon film is often not ideal for non-crystalline single particles as it adds background to an image and can induce preferred particle orientation.

We have recently investigated an imaging protocol in which the electron dose rate was varied, to image single particles embedded in ice over holes in a carbon support film (Chen et al., 2008). These experiments suggested that a lower dose rate allows for a higher total dose before bubbling occurs, but did not clearly demonstrate that beam-induced motion prior to bubbling was reduced. In the present study, we have investigated beam-induced motion by monitoring positions and orientations of rotavirus double-layer particles (DLPs). These particles are very regular and have a molecular mass of 70 MDa, allowing alignment with a reference structure with accuracies of about 0.2 Å and 0.2°, for translational and orientational alignments, respectively (Zhang et al., 2008). We collected exposure series from holes inside perforated carbon films containing rotavirus embedded in ice, varying dose rate and hole size. Changes in the particle orientations between exposures were then taken as an indication for specimen motion. In a second set of experiments, we investigated the timing of the beam-induced motion during exposures by recording movies using a new type of camera, a direct electron detector. Particles visible in individual frames or frame averages were analyzed in terms of their orientational and translational changes during the exposure.

2. Materials and methods

2.1. Sample preparation

Rotavirus DLPs were prepared as described (Street et al., 1982). Three microliters of sample with a concentration of 2.5–4 mg/ml was applied to Quantifoil® or C-flat™ grids and plunge-frozen using either a Gatan CP3 plunger (for all exposure series experiments) or an FEI Vitrobot Mark 2 (for all movie experiments), with a 4 or 6 s blot time and at relative humidity between 65% and 80%. The following grid types were used: Quantifoil® 1.2/1.3 Cu 400 mesh (measured hole size = 1.6 μm; this difference between nominal and measured hole size was observed for all grids in this batch), C-flat™ 0.6/2.0 Cu 400 mesh (measured hole size = 0.6 μm), C-flat™ 1.0/1.0 Cu 400 mesh (measured hole size = 1.0 μm), and C-flat™ 1.2/1.3 Cu 400 mesh (measured hole size = 1.2 μm). The Quantifoil® grids were cleaned prior to their use by immersion in a small amount of ethyl acetate on top of filter paper in a glass Petri dish. Immediately before plunging, all grids were subject to glow discharge for 45 s at 20 mA.

2.2. Electron microscopy – exposure series

Images were collected on a Gatan US4000 4 k × 4 k CCD camera mounted on an FEI TF30 electron microscope operating at 300 kV, and using a side-entry Gatan 626 cryo holder. The calibrated magnification was 49,053, giving a pixel size on the specimen of 3.06 Å. Magnification calibration was performed using a DLP reference structure (Zhang et al., 2008) and maximizing correlation coefficients found by varying the pixel size during *Frealign* (Grigorieff, 2007) runs (see below). We used an underfocus of 2.5–3.5 μm, and an electron dose per exposure of 8 electrons/Å². Images in each series were taken about 60 s apart, and occasionally 600 s apart to test if charging was a factor in the observed particle motions (see Section 3). The exposed area on the grid was centered on each hole and held approximately constant at 2.0 μm to ensure that the electron beam made contact with the carbon support film everywhere around holes. Furthermore, an objective aperture was used for all exposures. The ice thickness was measured using holes in the ice layer produced by a focused electron beam with subsequent tilting to 30° (Wright et al., 2006). The ice next to virus particles was determined to be between 800 and 1000 Å thick while it was thinner in the center of holes, with the thinnest ice (500 Å) measured in the center of 1.6 μm holes on Quantifoil® grids.

2.3. Electron microscopy – movies

Images were collected on a Direct Electron DE-12 4 k × 3 k direct electron detector mounted on an FEI TF20 electron microscope operating at 200 kV, and using a side-entry Gatan 626 cryo holder. The calibrated magnification was 17,858, giving a pixel size on the specimen of 3.36 Å. The underfocus was set between 2.5 and 3.5 μm, and the electron dose per frame was 0.5 electrons/Å². Movies were recorded at a rate of 40 frames/s. The exposed area was adjusted as above and ice thickness measurements were essentially identical to those measured above.

2.4. Image processing – exposure series

Virus particles were semi-automatically selected from the first image in an exposure series using *e2boxer* from the *EMAN2* processing package (Tang et al., 2007). Micrographs were cross-correlated to each other using the *Spider* processing package (Frank et al., 1996) to determine translational offsets, and particles were selected in subsequent exposures by coordinates updated with the offsets. The defocus for each micrograph was determined using *CTFFIND3* (Mindell and Grigorieff, 2003). Particle images were decimated using 2 × 2 pixel averaging and aligned in an exhaustive search with *Frealign* (Grigorieff, 2007) (Mode = 4 with DANG = 200 and IT-MAX = 200 using data between 18 and 300 Å resolution), followed by 10 rounds of refinement (Mode = 1), using a DLP reference structure (Zhang et al., 2008). The rotation angles and axes of reorientations experienced by particles between exposures were determined using the program *Tiltdiff* (Henderson et al., 2011). The rotation axis of most particles was within 0.5° in the image plane. About 6% of the particles were measured to have tilt axes with larger out-of-plane angles. These were excluded from the analysis to eliminate cases were the exhaustive parameter search failed. Histograms of the magnitude of the measured rotation angles were generated with a bin size of 0.1°. The histograms show a clear positive skewness, indicating that a simple average and standard deviation might not be appropriate to characterize the distribution of rotation angles. We used the computer program *distfit* from the *Theseus* package (Theobald and Wuttke, 2006) to test 20 different distributions and selected the Rayleigh distribution as the most appropriate according to the Bayesian information criterion. The Rayleigh distribution (Lalitha and Mishra, 1996) is characterized by a single parameter, λ which indicates the maximum (mode) of the distribution:

$$R(x; \lambda) = \frac{x}{\lambda^2} e^{-x^2/2\lambda^2}. \tag{1}$$

The maximum likelihood estimate of λ^2 is:

$$\lambda^2 = \frac{1}{2N} \sum_{i=1}^{N} x_i^2 \tag{2}$$

Table 1
Rotation angles measured between the first and second exposures in exposure series of rotavirus particles in vitrified ice over holes in perforated carbon support films. The dose per exposure was 8 electrons/Å². The dose rate was varied from 2 electrons/Å²/s – 160 electrons/Å²/s and support films with different hole sizes, varying from 0.6 to 1.6 μm were used.

Dose Rate	Hole = 0.6 μm	Hole = 1.0 μm	Hole = 1.2 μm	Hole = 1.6 μm
2 e⁻/Å²/s	0.412 ± 0.015 ($N = 187$)	0.413 ± 0.014 ($N = 211$)	0.394 ± 0.008 ($N = 599$)	0.470 ± 0.008 ($N = 783$)
20 e⁻/Å²/s	0.460 ± 0.013 ($N = 307$)	0.403 ± 0.013 ($N = 257$)	0.384 ± 0.006 ($N = 879$)	0.608 ± 0.010 ($N = 919$)
80 e⁻/Å²/s	0.453 ± 0.013 ($N = 302$)	0.415 ± 0.013 ($N = 261$)	0.443 ± 0.007 ($N = 889$)	0.481 ± 0.009 ($N = 694$)
160 e⁻/Å²/s	0.480 ± 0.017 ($N = 210$)	0.433 ± 0.014 ($N = 255$)	0.461 ± 0.010 ($N = 538$)	0.558 ± 0.011 ($N = 678$)

and standard error in λ^2 is:

$$SD(\lambda^2) = \frac{\lambda^2}{\sqrt{N-1}}. \tag{3}$$

Therefore, standard error in λ^2 is:

$$SD(\lambda) \approx \frac{SD(\lambda^2)}{2\lambda} = \frac{\lambda}{2\sqrt{N-1}}. \tag{4}$$

This error is reported together with λ in Table 1 for the fitted distributions.

2.5. Image processing – movies

Raw movie frames were corrected for dark current and gain-normalized using dark frames and flat fields recorded directly before each movie and at the beginning of a session, respectively. Frame averages were calculated using the computer program *label* from the MRC image processing package (Crowther et al., 1996). Particle rotations and translations were analyzed using *Frealign* as described above, except using data between 25 and 800 Å.

3. Results

3.1. Exposure series

In a first set of experiments we investigated the influence of dose rate on beam-induced motion using exposure series. Fig. 1A shows a field of rotavirus particles prepared using C-flat™ 1.2/

1.3 Cu 400 mesh grids (hole size = 1.2 μm). The image was recorded using a dose rate of 20 electrons/Å²/s and the exposure lasted 0.4 s, giving a total dose of 8 electrons/Å². Subsequent exposures are shown in panels B–D, indicating no bubbling in the sample even in the final exposure, after which the total dose was 32 electrons/Å². Virus particles are clearly visible in all exposures and could readily be aligned using a reference structure (Zhang et al., 2008). Using projection matching implemented in the computer program *Frealign* (Grigorieff, 2007), the orientation of most of the virus particles in all four exposures were determined successfully, as judged by their small angular differences and small out-of-plane errors (see Materials and methods) determined by the program *Tiltdiff* (Henderson et al., 2011). The angular differences between exposures are plotted as vectors in panels E–G to show both the magnitude and direction of the rotations. A striking feature of these plots is the local correlation in the rotation vectors, extending over a distance of 300–500 nm. This correlation also indicates that most particle orientations were determined correctly within a degree or better. Furthermore, it shows that the orientation changes between exposures is not due to the motion of individual virus particles in the ice, but that it must be due to a deformation in the ice layer itself, moving the particles with it. The angular changes of up to 2° seen in panel E were also observed in many other exposure series. The direction of the rotation reverses from one side of the hole to the other, indicating that the ice undergoes a drum-like motion with a curvature radius of 25 μm and translation of the central region perpendicular to the specimen plane of about 150 Å (see Section 4). Subsequent exposures produce further particle rotations approximately in the same
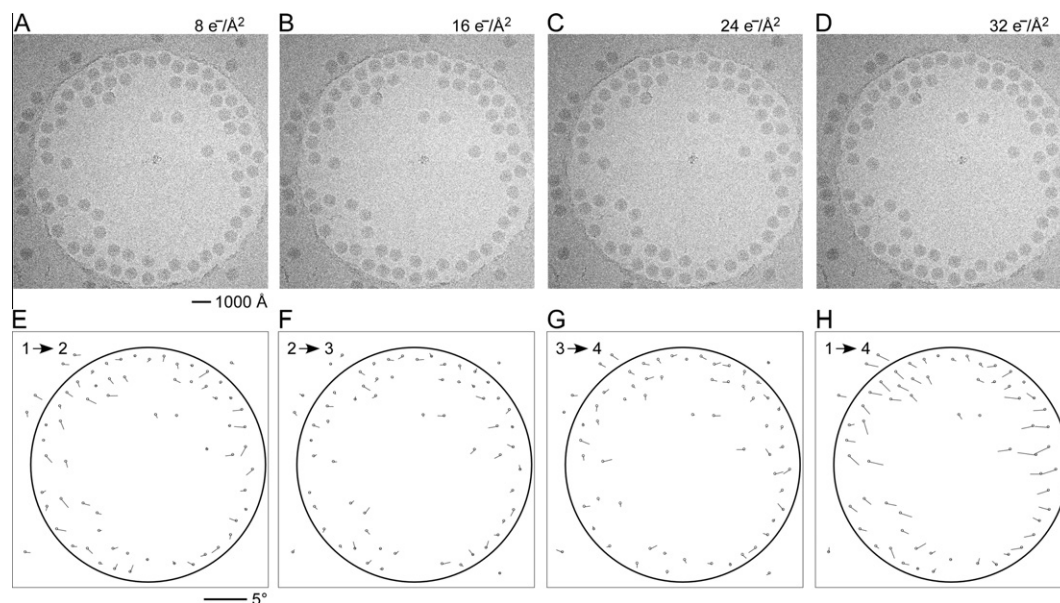

Fig.1. Exposure series of rotavirus DLPs in ice in a C-flat™ 1.2/1.3 grid (hole size = 1.2 μm). Four successive exposures are shown in panels A, B, C and D. The total dose applied to the sample is noted above each exposure. Panels E, F and G show vector plots corresponding to the changes in particle orientations between exposures (exposure numbers are indicated in the plots). Panel H plots the summed vectors from panels E, F and G.

direction but their magnitude decreases, suggesting that beam-induced motion is largest during the initial exposure, and that it is dose-dependent. The particle rotations observed in the ice also apply to the few virus particles found on the carbon next to the hole in Fig. 1, indicating that the motion in the ice extends into the neighboring carbon support film.

We observed the same pattern of correlated particle rotations in many other exposure series, with vectors pointing either away from or towards the center of the hole, indicating that the direction of the drum motion is random. Furthermore, the magnitude of the observed rotations varied considerably from series to series. To gain a more quantitative understanding of the orientation changes, and to investigate the influence of dose rate and hole size, we recorded exposure series from 438 holes on 11 grids, yielding a total of 8089 DLPs for rotation measurements. The dose rates used were 2, 20, 80 and 160 electrons/$Å^2$/s. To vary the hole size, we used Quantifoil® grids (1.6 µm holes), as well as C-flat™ grids (0.6, 1.0 and 1.2 µm holes). Fig. 2 shows the histograms of measured rotations between the first and second exposures for all tested dose rates and a hole size of 1.2 µm. To interpret the histograms, we calculated maximum-likelihood fits of the Rayleigh distribution (see Materials and methods). The fitted Rayleigh distributions are superimposed on each histogram in Fig. 2, and their distribution maxima are given in Table 1 (for all conditions tested), together with their standard errors and the number of particles analyzed. The results in Fig. 2 and Table 1 show that the magnitude of particle motion is quite variable and that alterations in dose rate and hole size do not produce predictable changes in the particle motions. Clear trends are discernible, however. Particles suspended over larger holes show larger rotations than particles in smaller holes. Thus, the largest average rotations for all dose rates were observed with 1.6 µm holes (Quantifoil® grids) while the rotation averages determined for 1.0 µm holes (C-flat™ grids) were equal (within error estimates) or smaller than those seen with 1.2 µm holes (C-flat™ grids). The results for 0.6 µm holes do not appear to follow this trend which may reflect irregular hole boundaries and/or a larger contribution of the carbon support to the overall motion (see Section 4). There is also a clear trend with dose rate, showing larger rotations as the rate increases, with the highest rate (160 electrons/$Å^2$/s) producing the largest average rotations in most cases. We also varied the time between exposures between 60 and 600 s but did not detect noticeable changes in the magnitude of beam-induced motion. Analysis of rotations in subsequent exposures generated similar histograms with rotations of somewhat reduced but still significant magnitude, in agreement with the observations shown in Fig. 1.

3.2. Movies

Particle rotations of a few degrees during beam exposure result in movement of peripheral density features of the 700 Å virus particles by 10 Å or more, thereby eliminating any signal at sub-nanometer resolution in the direction of rotational movement. Since cryo-EM data recorded under similar conditions led to a reconstruction of the peripheral rotavirus coat proteins at 3.8 Å resolution (Chen et al., 2009; Settembre et al., 2011; Zhang et al., 2008) the observed particle rotations must occur in such a way that significant high-resolution signal is preserved. The rotation vectors suggest that the rotation for any given particle occurs around an approximately fixed axis. Subunits closer to the rotation axis will move less than those further away from the axis (see Discussion and conclusions), thereby maintaining stronger high-resolution contrast in the images. Other particles may not move much at all, as indicated by the histograms in Fig. 2, and will exhibit even stronger high-resolution contrast. It is also possible that the particle rotations do not occur at a constant rate during the exposure. For example, if particles rotate more rapidly initially and then slow down during an exposure, blurring in the final image would be less severe compared to blurring produced by particles that rotate at a constant rate.

To investigate the timing of the motion, we recorded movies at 40 frames/s of virus specimens prepared using Quantifoil® grids as these showed the largest beam-induced motions (see Supplementary material). At a dose rate of 20 electrons/$Å^2$/s, the dose per frame is only 0.5 electrons/$Å^2$, too low to produce sufficient contrast for particle alignment (Movie S1). We therefore calculated 10-frame averages to improve the contrast while still allowing a temporal resolution of 0.25 s/averaged frame (Movies S2 and S3). We also made sure that we captured the onset of the exposure by starting recording before the beam shutter (above the specimen) was opened. Therefore, the first few frames of a movie contain dark frames. Fig. 3 shows results for a 1.5 s exposure with
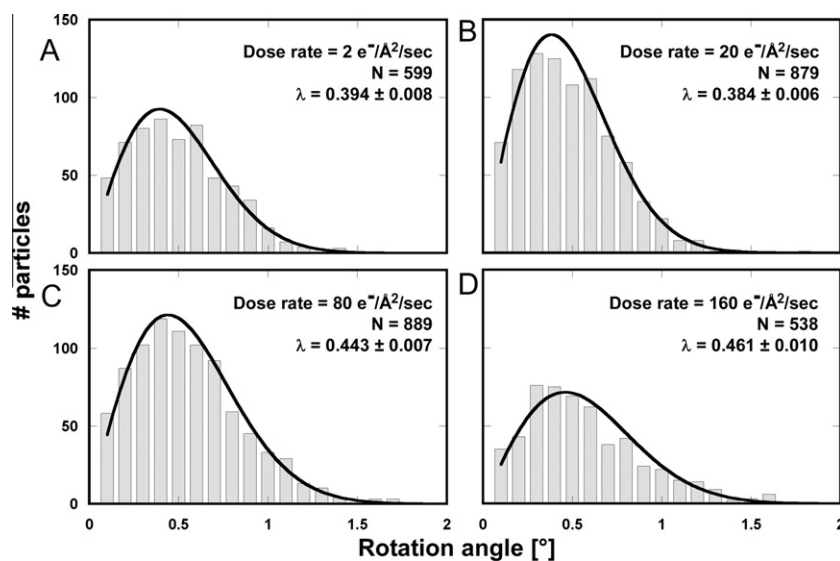

Fig. 2. Histograms for particle rotations measured between the first and second exposures of rotavirus DLPs in ice on C-flat™ 1.2/1.3 Cu 400 mesh grids (hole size = 1.2 µm). The dose applied in each exposure was 8 electrons/$Å^2$. The dose rate varied between 2 and 160 electrons/$Å^2$/s, giving exposure times between 0.05 and 4 s. The histograms were fitted with a Rayleigh distribution and maximum (λ) is indicated in each plot together with the total number of measurements.

63 raw frames (Movie S1) of which the first three frames were dark. The vector plots in Fig. 3A–E indicate the incremental rotations between 10-frame averages (see corresponding Movie S2). The plots exhibit the same overall pattern as those produced from the exposure series, with local correlations and opposite directions on opposite sides of the hole. As the exposure progresses, rotation increments become smaller until they are frequently within the detection limit of our method (rotations smaller than about 0.2°). The rotation vectors suggest smaller rotations for particles closer to the center of the hole, consistent with the above-mentioned drum-like motion, which predicts a larger rotational motion near the edge. The largest overall rotational motion during the 1.5 s exposure of the movie is about 4°, suggesting that the drum motion in the center of the hole could be up to 250 Å perpendicular to the specimen plane, producing a curvature of the ice layer with a

12 μm radius. The rotations seen in the movies are larger than those we observed with most of the exposure series. However, in the exposure series we were not able to observe the full extent of the rotations at the beginning of an exposure, only the average orientation over its entire duration. The larger rotations seen in the movies therefore do not contradict the results from the exposure series.

We also analyzed the incremental shifts of each particle, shown in Fig. 3G–K (see corresponding Movie S3). The largest overall translational motion is about 70 Å (Fig. 3L), part of which may be attributable to the drum motion (see Discussion and conclusions). Unlike the rotations, the particle translations are not distributed roughly symmetrically around the center of the hole. Instead, translations in the upper right corner are larger than elsewhere in the hole. Inspection of the movies (Supplementary material, Movies S2 and S3) shows that the edge of the carbon moves in the same direction as the adjacent particles. The larger translations are directed towards the center of the hole, suggesting that the hole contracts in the direction of the translations (along the diagonal from the bottom left to the top right of the image) and that the distances between particles in the image decrease. We found similar patterns of translation in many other movies. A reduction in distance was also observed previously in images of gold particles in ice (Chen et al., 2008) and is most consistent with a drum motion of the ice layer that is induced by a shrinking dimension of the hole, rather than an expansion of the ice. Hence, deformation of the carbon support film contributes to the overall particle motion, consistent with the observed rotation of the virus particles found on the carbon next to the hole in Fig. 1.
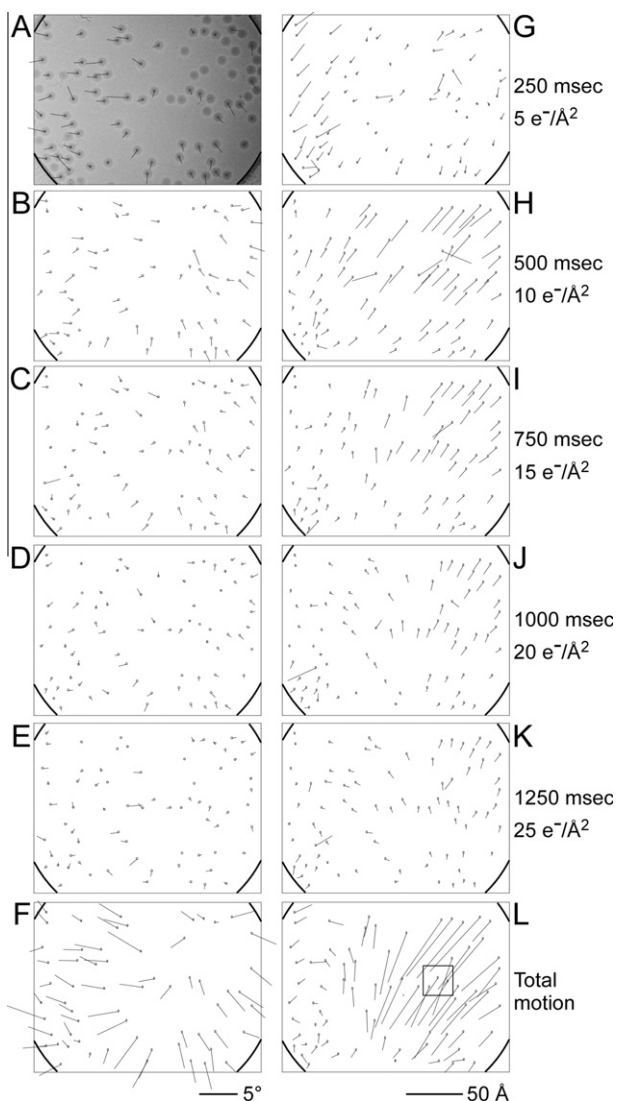
4. Discussion and conclusions

4.1. Beam-induced motion is caused by changes in the ice layer and carbon support film

Beam-induced specimen motion has long been recognized as one of the main factors attenuating high-resolution signal in cryo-EM (Bottcher, 1995; Bullough and Henderson, 1987; Glaeser et al., 2011; Henderson, 1992). The main cause of this motion is beam damage occurring to the specimen as it is exposed to the high-energy electron beam (Glaeser, 2008; Glaeser and Taylor, 1978; Glaeser et al., 2011) although charging may also play a role (Glaeser and Downing, 2004; Henderson, 1992). Increased mechanical stability of the continuous support film used with 2D crystals reduces or entirely avoids beam-induced motion, but an equivalent solution has not yet been found for single particles suspended in ice layers over holes in the perforated carbon film. In the present study we investigated the nature of beam-induced motion of particles in ice over holes. Our analysis of images obtained during an exposure series indicates that the ice inside the holes undergoes drum-like motion with a curvature radius of 12–25 μm and translation of the central region perpendicular to the specimen plane of 150–250 Å. In earlier studies, it was observed that the ice layer spanning the holes in perforated carbon films assumes a dome shape (Wright et al., 2006). This is consistent with the present study, which implies that the observed dome shape was at least partially induced by a drum motion. It is likely that this drum motion is caused to some extent by an increase in internal pressure in the ice due to the molecular radicals generated by radiolysis, leading to an expansion of the ice layer as previously suggested (Glaeser, 2008). However, a significant amount of additional motion is produced by changes in the carbon support film. This is clearly indicated by the particle translations during beam exposure shown in Fig. 3. The changes appear to be anisotropic, reducing the hole dimension predominantly in one direction. The hole analyzed

Fig.3. Movie frame averages of rotavirus DLPs in ice on a Quantifoil® grid (hole size = 1.6 μm). The movie was recorded for 1.5 s at 40 frames/s using the DE-12 direct electron detector (Direct Electron). 10-frame averages of the resulting 60 frames were subjected to the same analysis as the exposure series. Vector plots in panels A–E indicate particle rotations measured between frame averages. The total average of the movie is shown in the background in A and the summed rotations from panels A–E are shown in F. Panels G–K show vector plots indicating the particle translations measured between frame averages. Panel L shows the summed translations from panels G–K. The square highlights the area shown as a close-up in Fig. 5. The movie is further analyzed in Supplementary material (Movies S1–S3).

in Fig. 3 changes its dimension by about 50 Å (about 0.3%) in the direction of the largest translations. In the case shown in Fig. 3, the main cause of the observed beam-induced motion must therefore be due to changes in the carbon support. It is unlikely that these changes are the result of specimen heating by the electron beam which are estimated for a dose rate of 20 electrons/Å²/s to be between 0.2 K (Egerton and Rauf, 1999) and 0.5 K (Dietrich et al., 1978), leading to motions between 0.03 and 0.05 Å (assuming a thermal expansion coefficient of amorphous carbon of 5×10^{-6}/K, Booy and Pawley, 1993; Vonck, 2000) over a length of the beam diameter (2 μm). Instead, the changes may affect the atomic structure of the support film and explain why pre-irradiation of the support film (before application of the sample) with an electron beam may reduce beam-induced motion (Ge and Zhou, 2011; Miyazawa et al., 1999) (see below). Additional experiments are required to quantify how much beam-induced motion can be reduced by pre-irradiation of the carbon support, and to determine if a support film with higher mechanical stability (Glaeser et al., 2011) could also reduce the motion of the particles in the holes.

4.2. Deformations in the ice and carbon layers are plastic

The total dose used in the movie in Fig. 3 was 30 electrons/Å². Our experiments with exposure series indicate that subsequent exposures further increase the particle rotations, and with it the drum motion. The amount of motion therefore depends on the total dose applied to the sample. On the other hand, variation of the time between exposures did not significantly alter the amount of motion. This is inconsistent with a mechanism of beam-induced motion that depends on the build-up of charge on the specimen. Although we expect charging to occur as with any other cryo specimen, the charge drains after a few minutes (Brink et al., 1998). It is therefore likely that the deformation of the ice layer and carbon support is predominantly plastic, as one might expect for amorphous media such as vitrified ice and amorphous carbon. Since dose rate affects the magnitude of the motion, it appears that a lower dose rate reduces the strain induced in the specimen somewhat. The origin of the strain is not entirely clear. As previously discussed (Glaeser, 2008), radiolysis of the water and macromolecules likely leads to increased pressure inside the ice layer. A lower dose rate may reduce the pressure by giving molecular radicals more time to diffuse to the ice surface where they are released into the microscope vacuum. However, the carbon support is much more resistant to radiolysis and the induced strain in the carbon must have a different origin. The effectiveness of pre-irradiation in reducing beam-induced motion suggests that the electron beam has an 'annealing effect' on the carbon layer, allowing it to relax into a more stable configuration. The annealing will also depend on the energy input by the beam and hence the dose rate. Both processes (pressure increase due to radiolysis, relaxation by annealing) are consistent with the initial larger motion at the beginning of the exposure, followed by gradual relaxation into a new state that is stable under the beam. In this new state, the ice layer will have undergone a drum-like motion, producing the observed particle rotations and translations. When the exposure ends, the concentration of radicals will drop again, presumably leading to some relaxation of the ice layer. However, as the results from the exposure series show, this does not restore the latter to its original state as the annealing of the carbon and the straining of the ice lead to plastic deformation. Renewed exposure to the electron beam restarts the process and produces motion almost as large as the first exposure. As the specimen is repeatedly exposed (or exposed for a long time) to the electron beam, annealing of the carbon will progress to a more stable state. The events occurring during beam exposure are summarized in the schematic in Fig. 4.
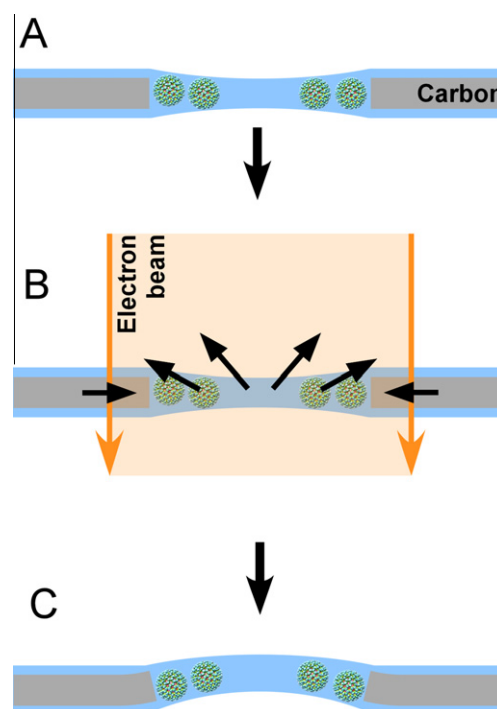

Fig.4. Schematic of beam-induced motion. (A) Particles are suspended in vitrified ice over a hole. (B) When the electron beam illuminates the sample, the carbon support film deforms such that the size of the hole shrinks by a small amount. At the same time, radiolysis of the solvent and macromolecules produces radicals that increase the pressure inside the ice layer. Both changes cause a drum motion of the ice layer that lead to particle rotations and translations. The direction of the drum motion is random. (C) After the beam is turned off, the changes induced in the specimen remain (plastic deformation). This model does not consider specimen charging which could add to the blurring of images.

4.3. Loss of high-resolution contrast is caused by particle rotation and translation

There is considerable variability in the amount of motion observed between different experiments (see Fig. 2), on average about 0.3°. The high-resolution detail will therefore be better preserved for some particles compared with others. The variability is presumably due to small random differences between holes and the ice in them. Further variability is due to the drum motion, which will lead to little or no particle motion in the center of the hole if it occurs perpendicular to the image plane, while rotations and some translations will be noticeable for particles closer to the edge of the hole. If the specimen is tilted with respect to the image plane, the drum motion will produce additional translations and hence blurring. For example, if the specimen is tilted by 30°, the translation in the image plane will be 75–130 Å for a drum motion of 150–250 Å, sufficient to obliterate all high-resolution contrast. Even at a small tilt angle of 3° which can occur unintentionally (Vonck, 2000), the translation in the image plane is still 7–13 Å, which will produce blurring corresponding to a temperature factor (B-factor) of about 4000–13,000 Å² (Jensen, 2001) (B-factors are given in X-ray crystallographic notation). Additional blurring arises due to particle rotations. If we assume an average rotation angle of 2° we expect the signal of coat molecules within a radius of about 100 Å from the axis to be attenuated by a B-factor of about 450 Å² (Jensen, 2001), which is the average B-factor determined for the reference rotavirus reconstruction (Zhang et al., 2008). The surface area near the rotation axis included within this radius is about 1/50 of the total area. Therefore, if rotation alone were responsible for the signal loss, we would expect to obtain a resolu-

tion of 3 Å from images of 50,000 to 500,000 molecules, still less than what has been observed in the recent virus reconstructions at near-atomic resolution. The blurring factor due to translation can easily account for the additional loss of signal to account for the observed requirement of several 100,000 to over 10 million molecules (Grigorieff and Harrison, 2011).

4.4. Beam-induced motion depends on hole size and dose rate

We have previously shown that a reduced dose rate increases the total dose needed to observe bubbling in the specimen (Chen et al., 2008), prompting us to examine the effect that dose rate has on beam-induced motion. Furthermore, the importance of mechanical stability observed with 2D crystals led us to include in our study specimens with different hole sizes in the support film. Our measurements suggest that neither dose rate nor hole size can be adjusted to avoid beam-induced motion entirely. However, lower dose rates and smaller holes appear to reduce motion on average while the largest rotations are observed with 1.6 μm holes. Apart from their larger size, the ice layers in the 1.6 μm holes also exhibit the greatest variation in thickness, 1000 Å near the edge and 500 Å in the middle. The thinner ice regions may be more susceptible to deformation than the thicker regions, allowing larger deformations in larger holes (Yoshioka et al., 2010).

Measurements made with the smallest hole size of 0.6 μm represent an exception of the observed trend as the average rotations are larger than those observed with 1.0 and 1.2 μm in most cases. A possible reason might be the frequently observed irregular edges of the 0.6 μm holes (Figure S1) which may contribute to the mechanical instability of the specimen. Furthermore, as the size of the illuminated area for all hole sizes was kept approximately constant (2 μm diameter), there was more carbon within the area. It is therefore possible that the instabilities of the carbon support film discussed above and observed previously (Glaeser et al., 2011) contributed to the larger particle rotations inside the 0.6 μm holes.

4.5. Movie frame alignment and averaging can reduce blurring in the images

There has been a common belief that beam-induced motion is worst at the beginning of the exposure. The movie in Fig. 3 shows that this is indeed the case and that the first 10 electrons/Å^2 cause about twice as much motion (about 2.5°) as the following 20 electrons/Å^2 (about 1°). The analysis of other movies yielded essentially identical results in terms of the temporal behavior of beam-induced motion. If beam-induced motion cannot be avoided,

the high-resolution signal might be boosted somewhat if 5–10 electrons/Å^2 dose are accumulated on the specimen before the camera shutter is opened. However, movies of the particle motions may make it possible to avoid image blurring entirely. If the direction, magnitude and timing of the particle translations and rotations during the exposure can be determined, particle images from individual frames could be averaged with their correct orientations and positions, thus preserving the high-resolution signal. This will require low-noise image recording, a feature that is becoming available with the latest generation of direct electron detectors (McMullan et al., 2009; Milazzo et al., 2011, 2005). A further requirement will be sufficient signal in frame averages of the movies to determine the translations and rotations taking place during the exposure. For the 70 MDa virus particle used in our studies, images with a combined dose of 5 electrons/Å^2 at 200 kV (10-frame averages) were sufficient. Using the translations determined in Fig. 3, we performed frame alignment for a small area of the hole with three virus particles (Fig. 5). Compared to the average in Fig. 5A calculated without alignment, the average with alignment in Fig. 5B shows a substantial reduction of blurring. Blurring due to the particle rotations cannot be removed by simple 2D alignment but could be corrected for by appropriate adjustment of the Euler angles in a 3D reconstruction from individual movie frames.

For particles with smaller molecular mass, such as the 70S ribosome (2.6 MDa), the signal in the images will be weaker and it might be necessary to add larger particles, such as the rotavirus particles used here, to enable tracking of the ice layer. However, since their radius is also smaller, which reduces the blurring of peripheral regions compared to the virus particles examined here, the effect of particle rotation on the final 3D map will be less. For example, the 70S ribosome has a diameter of about 250 Å, suggesting that an angular accuracy of 0.6° would be sufficient to obtain a reconstruction at 4 Å resolution. Therefore, although tracking of the ice deformation would still be necessary to reduce blurring by the expected beam-induced particle rotations, the required accuracy is not as high as with the virus particles.

4.6. Other factors may play a role in beam-induced motion

We have investigated here only two factors with a possible influence on beam-induced motion, namely dose rate and hole size (within a limited range of sizes from 0.6 to 1.6 μm). Much smaller holes (with more regular edges and illuminated with a beam with smaller diameter) and dose rates may be required to achieve a more significant reduction of beam-induced motion than observed
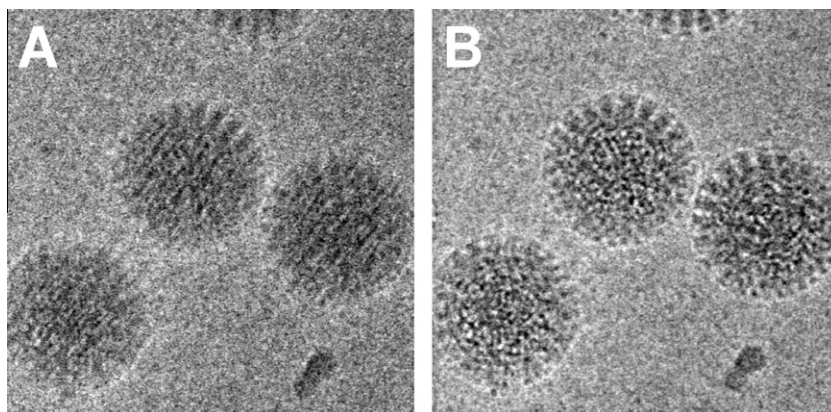

Fig.5. Translational alignment of movie frames to reduce blurring in images affected by beam-induced motion. (A) Average of 60 frames of an area of Movie S1 that experienced translations of about 60 Å (see Fig. 3L) Particles are significantly blurred and high-resolution information is lost. (B) Average of the same 60 frames as in panel A after translational alignment of individual frames. The translations for the individual frames were calculated from the translations determined in Fig. 3 for the 10-frame averages by linear interpolation. The frame average in panel B exhibits substantially improved contrast with details at higher resolution that were not visible in panel A.

in our experiments. Other factors that may be important include carbon thickness, pre-irradiation of the carbon support, size of the illuminated area, ice thickness, ice uniformity, protein density, buffer composition, as well as additives that may stabilize the ice layer or act as sinks for the molecular radicals produced by radiolysis. Although the processing of movies tracking the ice layer deformation may be one way to reduce the deteriorating effect of beam-induced motion of the high-resolution data, it would be more desirable for practical reasons to reduce or eliminate beam-induced motion altogether. Our results show that large virus particles such as rotavirus used here provide effective probes to monitor and quantify beam-induced motion. These particles therefore represent a valuable new tool to investigate beam-induced motion further and identify procedures that help preserve high-resolution detail in cryo-EM images.

Acknowledgments

Appendix A. Supplementary data

Supplementary data associated with this article can be found, in the online version, at doi:10.1016/j.jsb.2012.02.003.

References

Baker, L.A., Smith, E.A., Bueler, S.A., Rubinstein, J.L., 2010. The resolution dependence of optimal exposures in liquid nitrogen temperature electron cryomicroscopy of catalase crystals. Journal of Structural Biology 169, 431–437.

Booy, F.P., Pawley, J.B., 1993. Cryo-crinkling: what happens to carbon films on copper grids at low temperature. Ultramicroscopy 48, 273–280.

Bottcher, B., 1995. Electron cryomicroscopy of graphite in amorphous Ice. Ultramicroscopy 58, 417–424.

Brink, J., Sherman, M.B., Berriman, J., Chiu, W., 1998. Evaluation of charging on macromolecules in electron cryomicroscopy. Ultramicroscopy 72, 41–52.

Bullough, P., Henderson, R., 1987. Use of spot-scan procedure for recording low-dose micrographs of beam-sensitive specimens. Ultramicroscopy 21, 223–229.

Cambie, R., Downing, K.H., Typke, D., Glaeser, R.M., Jin, J., 2007. Design of a microfabricated, two-electrode phase-contrast element suitable for electron microscopy. Ultramicroscopy 107, 329–339.

Chen, J.Z., Sachse, C., Xu, C., Mielke, T., Spahn, C.M., et al., 2008. A dose-rate effect in single-particle electron microscopy. Journal of Structural Biology 161, 92–100.

Chen, J.Z., Settembre, E.C., Aoki, S.T., Zhang, X., Bellamy, A.R., et al., 2009. Molecular interactions in rotavirus assembly and uncoating seen by high-resolution cryo-EM. Proceedings of the National Academy of Sciences of the United States of America 106, 10644–10648.

Crowther, R.A., Henderson, R., Smith, J.M., 1996. MRC image processing programs. Journal of Structural Biology 116, 9–16.

Danev, R., Nagayama, K., 2001. Transmission electron microscopy with Zernike phase plate. Ultramicroscopy 88, 243–252.

Dietrich, I., Fox, F., Heide, H.G., Knapek, E., Weyl, R., 1978. Radiation damage due to knock-on processes on carbon foils cooled to liquid helium temperature. Ultramicroscopy 3, 185–189.

Egerton, R.F., Rauf, I., 1999. Dose-rate dependence of electron-induced mass loss from organic specimens. Ultramicroscopy 80, 247–254.

Frank, J., Radermacher, M., Penczek, P., Zhu, J., Li, Y., et al., 1996. SPIDER and WEB: processing and visualization of images in 3D electron microscopy and related fields. Journal of Structural Biology 116, 190–199.

Ge, P., Zhou, Z.H., 2011. Hydrogen-bonding networks and RNA bases revealed by cryo electron microscopy suggest a triggering mechanism for calcium switches. Proceedings of the National Academy of Sciences of the United States of America 108, 9637–9642.

Glaeser, R.M., 1999. Review: electron crystallography: present excitement, a nod to the past, anticipating the future. Journal of Structural Biology 128, 3–14.

Glaeser, R.M., 2008. Retrospective: radiation damage and its associated "information limitations". Journal of Structural Biology 163, 271–276.

Glaeser, R.M., Taylor, K.A., 1978. Radiation damage relative to transmission electron microscopy of biological specimens at low temperature: a review. Journal of Microscopy 112, 127–138.

Glaeser, R.M., Downing, K.H., 2004. Specimen charging on thin films with one conducting layer: discussion of physical principles. Microscopy and Microanalysis 10, 790–796.

Glaeser, R.M., Hall, R.J., 2011. Reaching the information limit in cryo-EM of biological macromolecules: experimental aspects. Biophysical Journal 100, 2331–2337.

Glaeser, R.M., McMullan, G., Faruqi, A.R., Henderson, R., 2011. Images of paraffin monolayer crystals with perfect contrast: minimization of beam-induced specimen motion. Ultramicroscopy 111, 90–100.

Gonen, T., Sliz, P., Kistler, J., Cheng, Y., Walz, T., 2004. Aquaporin-0 membrane junctions reveal the structure of a closed water pore. Nature 429, 193–197.

Grigorieff, N., 2007. FREALIGN: high-resolution refinement of single particle structures. Journal of Structural Biology 157, 117–125.

Grigorieff, N., Harrison, S.C., 2011. Near-atomic resolution reconstructions of icosahedral viruses from electron cryo-microscopy. Current Opinion in Structural Biology 21, 265–273.

Henderson, R., 1992. Image contrast in high-resolution electron microscopy of biological macromolecules: TMV in ice. Ultramicroscopy 46, 1–18.

Henderson, R., 1995. The potential and limitations of neutrons, electrons and X-rays for atomic resolution microscopy of unstained biological molecules. Quarterly Reviews of Biophysics 28, 171–193.

Henderson, R., Baldwin, J.M., Downing, K.H., Lepault, J., Zemlin, F., 1986. Structure of purple membrane from halobacterium halobium: recording, measurement and evaluation of electron micrographs at 3.5 Å resolution. Ultramicroscopy 19, 147–178.

Henderson, R., Chen, S., Chen, J.Z., Grigorieff, N., Passmore, L.A., et al., 2011. Tilt-pair analysis of images from a range of different specimens in single-particle electron cryomicroscopy. Journal of Molecular Biology 413, 1028–1046.

Jensen, G.J., 2001. Alignment error envelopes for single particle analysis. Journal of Structural Biology 133, 143–155.

Lalitha, S., Mishra, A., 1996. Modified maximum likelihood estimation for Rayleigh distribution. Commun Stat Theory 25, 389–401.

Majorovits, E., Barton, B., Schultheiss, K., Perez-Willard, F., Gerthsen, D., et al., 2007. Optimizing phase contrast in transmission electron microscopy with an electrostatic (Boersch) phase plate. Ultramicroscopy 107, 213–226.

McMullan, G., Chen, S., Henderson, R., Faruqi, A.R., 2009. Detective quantum efficiency of electron area detectors in electron microscopy. Ultramicroscopy 109, 1126–1143.

Milazzo, A.C., Cheng, A., Moeller, A., Lyumkis, D., Jacovetty, E., et al., 2011. Initial evaluation of a direct detection device detector for single particle cryo-electron microscopy. Journal of Structural Biology 176, 404–408.

Milazzo, A.C., Leblanc, P., Duttweiler, F., Jin, L., Bouwer, J.C., et al., 2005. Active pixel sensor array as a detector for electron microscopy. Ultramicroscopy 104, 152–159.

Mindell, J.A., Grigorieff, N., 2003. Accurate determination of local defocus and specimen tilt in electron microscopy. Journal of Structural Biology 142, 334–347.

Miyazawa, A., Fujiyoshi, Y., Stowell, M., Unwin, N., 1999. Nicotinic acetylcholine receptor at 4.6 A resolution: transverse tunnels in the channel wall. Journal of Molecular Biology 288, 765–786.

Muller, H., Jin, J., Danev, R., Spence, J., Padmore, H., et al., 2010. Design of an electron microscope phase plate using a focused continuous-wave laser. New Journal of Physics, 12.

Sachse, C., Chen, J.Z., Coureux, P.D., Stroupe, M.E., Fandrich, M., et al., 2007. High-resolution electron microscopy of helical specimens: a fresh look at tobacco mosaic virus. Journal of Molecular Biology 371, 812–835.

Settembre, E.C., Chen, J.Z., Dormitzer, P.R., Grigorieff, N., Harrison, S.C., 2011. Atomic model of an infectious rotavirus particle. The EMBO Journal 30, 408–416.

Street, J.E., Croxson, M.C., Chadderton, W.F., Bellamy, A.R., 1982. Sequence diversity of human rotavirus strains investigated by northern blot hybridization analysis. Journal of Virological Methods 43, 369–378.

Tang, G., Peng, L., Baldwin, P.R., Mann, D.S., Jiang, W., et al., 2007. EMAN2: an extensible image processing suite for electron microscopy. Journal of Structural Biology 157, 38–46.

Theobald, D.L., Wuttke, D.S., 2006. THESEUS: maximum likelihood superpositioning and analysis of macromolecular structures. Bioinformatics 22, 2171–2172.

Vonck, J., 2000. Parameters affecting specimen flatness of two-dimensional crystals for electron crystallography. Ultramicroscopy 85, 123–129.

Wright, E.R., Iancu, C.V., Tivol, W.F., Jensen, G.J., 2006. Observations on the behavior of vitreous ice at approximately 82 and approximately 12 K. Journal of Structural Biology 153, 241–252.

Yonekura, K., Maki-Yonekura, S., Namba, K., 2003. Complete atomic model of the bacterial flagellar filament by electron cryomicroscopy. Nature 424, 643–650.

Yoshioka, C., Carragher, B., Potter, C.S., 2010. Cryomesh: a new substrate for cryo-electron microscopy. Microscopy and Microanalysis 16, 43–53.

Zhang, X., Settembre, E., Xu, C., Dormitzer, P.R., Bellamy, R., et al., 2008. Near-atomic resolution using electron cryomicroscopy and single-particle reconstruction. Proceedings of the National Academy of Sciences of the United States of America 105, 1867–1872.

Supplementary material for Brilot et al.

Beam-Induced Motion of Vitrified Specimen on Holey Carbon Film

Movie S1 63 raw movie frames. The pixel resolution of this movie was reduced by 8 x 8 pixel averaging for easier display, giving a pixel size on the specimen of 26.9 Å.

Movie S2 10-frame averages of Movie S1 with rotation vectors corresponding to the vectors shown in Figure 3A – E. The pixel resolution of this movie was reduced by 2 x 2 pixel averaging for easier display, giving a pixel size on the specimen of 6.72 Å.

Movie S3 10-frame averages of Movie S1 with translation vectors corresponding to the vectors shown in Figure 3F – J. The pixel resolution of this movie was reduced by 2 x 2 pixel averaging for easier display, giving a pixel size on the specimen of 6.72 Å.

Figure S1 Irregular edges in a 0.6 µm hole of a C-flat™ 0.6/2.0 Cu 400 mesh grid.